communications materials

A Nature Portfolio journal

Article

https://doi.org/10.1038/s43246-025-00988-9

Hydrogen uptake and embrittlement in nickel-base superalloys during hydrogen flame charging

Philipp Schulz [1,2], Dominik Dziedzic [1,2], Nuno Rocha [1], Chinonso Ezenwajiaku [1], Midhat Talibi [1], Ramanarayanan Balachandran [1] & Enrique Galindo-Nava [1]

Adopting hydrogen as fuel is one of the most promising solutions to eliminate carbon emissions in aviation. However, hydrogen is known to degrade the properties of structural alloys—a phenomenon known as hydrogen embrittlement. Here, we show that the environmental response of nickel-base superalloys in hydrogen combustion environments contrasts with the existing understanding of hydrogen embrittlement in metals. We demonstrate that direct flame exposure, i.e., flame charging, leads to significant hydrogen absorption, with oxidation strongly affecting hydrogen mass flow. Pre-existing oxides increase total hydrogen uptake during combustion, yet oxides also hinder hydrogen desorption. These effects reveal complex behaviour not observed in other hydrogen introduction methods, such as electrochemical hydrogen charging, with embrittlement being more extensive and showing distinct fracture behaviours. The study identifies key factors controlling hydrogen uptake and highlights critical differences between combustion and other hydrogen environments. Our findings can inform future alloy development, testing and certification for safe, sustainable hydrogen-powered jet engines.

Hydrogen has been used as a fuel in rocket applications since the late 1950s[1]. Now, more than six decades later and with carbon emissions continuously increasing, it has gained renewed interest in the aerospace industry as a promising technology to make medium- and long-haul flights sustainable. However, conditions between rocket engines and modern aero engines could not be more different: NASA's hydrogen-powered RS-25 space shuttle main engine was conceived to operate for approximately 9 minutes per flight with an overall lifespan of 8 hours[2]. In aviation, flight durations of 8 hours constitute a single long-haul flight, and turbofan engines have a service life in excess of 30,000 hours. Additionally, instead of using pure oxygen, as in the case of rocket engines, jet engines consume nitrogen-containing air, which introduces new environmental variables interacting with the surface of materials. Although previous investigations showed the general feasibility of hydrogen combustion in modified turbofan engines[3,4], there is little data available regarding the effect of this fuel on materials used in combustors and downstream components. An effect that is well known to occur in hydrogen-introducing environments is hydrogen embrittlement[5,6]. Structural alloys mechanically deformed after absorbing atomic hydrogen are known to suffer significantly reduced material ductility and strength compared to H-free conditions. As such, extensive studies have been conducted investigating the susceptibility of various Ni-base superalloys to embrittlement in gaseous hydrogen environments[7]. Nickel-base superalloys are precipitate-strengthened materials alloyed with elements including Al, Ti, or Nb to form coherent/semi-coherent particles known as γ' or γ'. This results in superior high-temperature creep and fatigue properties compared to other metals and therefore makes Ni-base superalloys the only materials suitable to operate in the most thermally and mechanically demanding parts of aero engines. The majority of studies conducted by NASA on such alloys were done using high-pressure (pure) hydrogen gas at room temperature and the applicability of this data on hydrogen combustion environments is yet to be determined. This is exacerbated by the fact that hydrogen embrittlement is likely not the only combustion-related effect that may promote material damage and early failure in these new engine environments. For example, considering the lower heating value of hydrogen compared to carbon fuels, a higher gas flow for hydrogen combustion engines may be necessary[8,9]; this coupled with the chemical reactions during H_2 combustion and air moisture likely contributes to a higher production of water steam. For Ni-base superalloys exposed to wet environments, it has been shown that water steam can promote enhanced growth and volatilisation of oxides, which can result in depletion zones below the surface, growth of internal oxides, or cracking and spalling[10–13]. Another effect that can be expected to negatively impact material performance during hydrogen

[1]Department of Mechanical Engineering, University College London, London, UK. [2]These authors contributed equally: Philipp Schulz, Dominik Dziedzic.
e-mail: e.galindo-nava@ucl.ac.uk

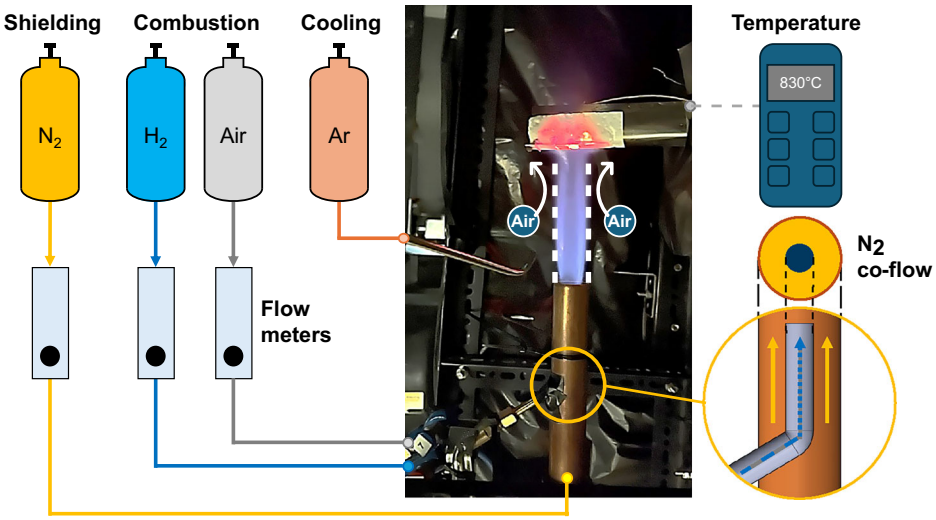

Fig. 1 | Schematic of the premixed flame combustion setup. Gas flow rates are set and monitored with flow metres. A nitrogen co-flow shields the flame from entrainment of atmospheric air.

combustion is a reduction in quenching distance compared to carbon fuel environments, that is, the separation between the flame and a cold wall at which flame extinguishment occurs[14,15]. This is therefore likely to result in an increase in thermal stress for H_2 combustion components compared to engines operating with carbon-based fuels.

In this work, we present -to the best of our knowledge- the first foundational series of experiments on the effect of hydrogen on Ni-base superalloys in representative engine environments. Our experiments focus on Inconel 718, which is the most widely used Ni-base superalloy both in rocket- and aviation applications. For this, we use a newly developed and custom-built hydrogen combustion rig for material testing, where test pieces are exposed to an H_2 flame under controlled combustion conditions, i.e., they are H_2-flame charged. We explore changes in hydrogen transport parameters with a prolonged exposure time of up to 8 hours to a hydrogen flame. This is achieved by using Thermal Desorption Analysis (TDA), which quantifies not only the total amount of hydrogen in a sample but also how much of that is diffusible within the bulk. We use Scanning Electron Microscopy (SEM) and tensile tests to analyse how combustion-related environmental conditions affect alloy microstructure and whether hydrogen embrittlement can actually occur in hydrogen combustion engines. We evaluate the performance of current Ni-base superalloys in an H_2 combustion environment and shed light on the key differences to electrochemical H charging. Thereby, we highlight the complex interactions between high-temperature hydrogen flame conditions and hydrogen-related phenomena, distinguishing our findings from previous literature. We are now able to obtain accurate and reproducible experimental data on the possible challenges faced by Ni-base superalloys in H_2 combustion aero engines by direct exposure to a hydrogen flame. These findings provide critical insights for the design, qualification, and certification of structural materials in hydrogen-powered combustion applications, where conventional testing methods fail to capture combustion-specific degradation mechanisms.

Results

Hydrogen Absorption Phenomena

Using our new custom-built combustion setup (Fig. 1), samples of Inconel 718 heat treated to peak-aged condition were hydrogen flame charged. Samples consist of (thicker) disc specimens -to focus on bulk alloy behaviour- and thin sheets -to enhance surface-related effects- both in polished and pre-oxidised conditions. The Supplementary information includes more detailed descriptions of the sample dimensions and methodologies used in this work. The effect of flame charging time to an H_2-rich flame on total hydrogen absorption and desorption is shown in Fig. 2a for disc specimens. To expand on where hydrogen is located in the samples, we conducted additional total hydrogen measurements in sheet specimens that are shown in Fig. 2b: Firstly, we quantified the total hydrogen in the oxide-containing alloy (circles) and in the bulk -no oxide- material (triangles) by removing the outside oxide layer; this is to ascertain the amount of hydrogen actually penetrating the scale. Secondly, we estimated the area under the curve of diffusible hydrogen measurements (squares), in which the sample is heated up to 900 °C at a constant rate and held for 10 minutes; the values help determine how much hydrogen is mobile within the sample during H combustion and that could potentially contribute to H embrittlement. To find the temperature at which hydrogen is released from the sample, we complemented total hydrogen measurements with diffusible hydrogen analyses (Fig. 2c). This approach allowed us to quantify both the hydrogen that becomes mobile -potentially contributing to hydrogen embrittlement- and the fraction that remains trapped at a given temperature condition.

In disc-shaped (bulk) specimens, an overall increase in total H occurs with exposure to the flame (Fig. 2a); results for both disc and sheet sample conditions follow a similar trend, but notable differences exist in the overall H values: Pre-oxidised disc samples have a distinctly higher H content (13.0 ± 1 ppm) compared to initially oxide-free specimens (9.5 ± 1 ppm) after 8 hours. In sheet samples, which were used to enhance surface effects, the measured hydrogen content is generally higher than in disc samples with the same pre-oxidised surface treatment (Figs. 2b and 6). In the first 4 hours, the average hydrogen concentration in the sheet samples increases to 29.5 ± 8 ppm, demonstrating more pronounced absorption when surface effects are amplified, as a result of the higher surface-to-volume ratio. Between 4 hours and 8 hours, the total hydrogen concentration decreases by more than 70%, to approximately 8.6 ppm, i.e., to a similar concentration as in oxide-free disc specimens. By removing the oxide scale after flame charging, we observe that the total hydrogen content remains virtually unchanged compared to samples with the oxide layer intact, across all three exposure durations (Fig. 2b). This shows that, in terms of the overall concentration, the vast majority of H is in fact contained in the bulk material. The analyses of hydrogen released up to 900 °C reveal that with a sample temperature of ~835 °C during the combustion trials, most H is diffusible and can diffuse across the surface layer. We also find that a small amount of hydrogen is released above 900 °C, which may be an indication of microstructural changes, a result of changes in oxide layer evolution or deep trapping.

To compare the hydrogen desorption profile from flame-charged samples to those from a charging method that is well established in the literature, we electrochemically charged additional specimens. To ensure that the profiles are comparable between the two environments, the charging time was chosen such that the amount of diffusible hydrogen, i.e., hydrogen that potentially contributes to H embrittlement, was of the same order of magnitude in both samples. Analysis of diffusible H in the electrochemically charged sample (blue line in Fig. 2c) confirms that, in this

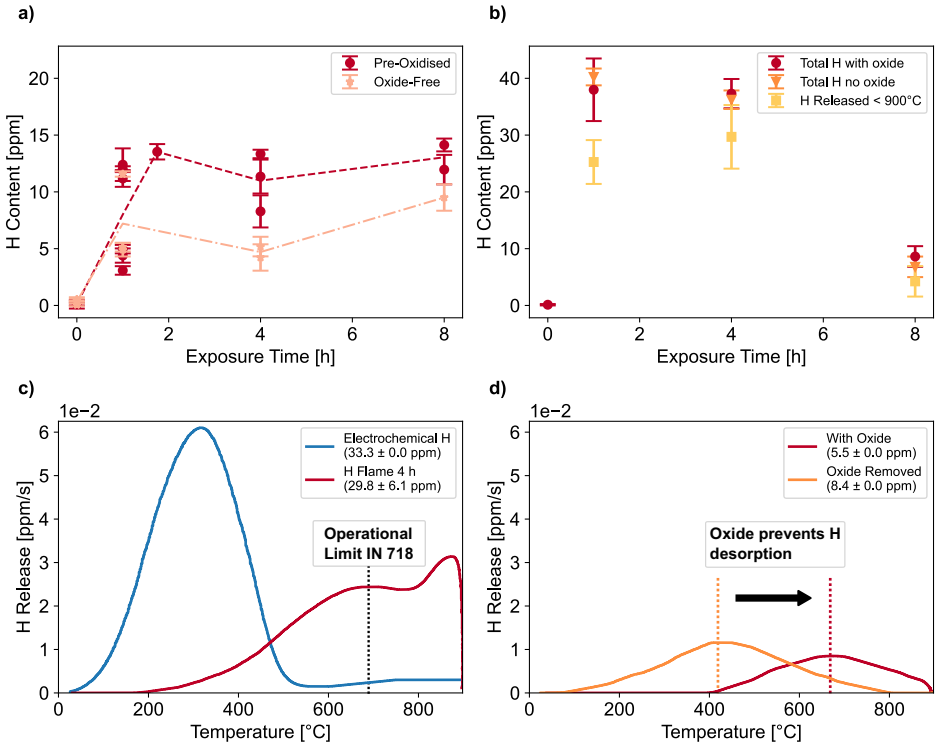

Fig. 2 | Hydrogen absorption and desorption phenomena. a Total hydrogen concentration in pre-oxidised and oxide-free samples over exposure time to the H_2 flame in 1 mm thick disc-shaped specimens. **b** Total H, total H in the bulk (no oxide), and total H released below 900 °C in pre-oxidised sheet samples. **c** Distribution of diffusible hydrogen in electrochemically charged and flame-exposed sheet samples. **d** Oxide scale as desorption-barrier in sheet samples H_2-flame charged for 1 h. Error bars in (**a**) and (**b**) represent measuring uncertainty from the TDA device.

case, most hydrogen is mobile within the crystal lattice. The TDA curve exhibits a distinct peak at 300 °C, with hydrogen release beginning at approximately 50 °C and minimal additional release observed after the peak. In contrast, the TDA curve of the sample flame charged for 4 h is shifted to the right. In this case, almost no hydrogen is picked up by the detector below 200 °C, with a first peak occurring at approximately 700 °C and a subsequent one at 850 °C. This high-temperature release of hydrogen could be mistaken as strong (bulk) H trapping behaviour, yet it is important to note that the flame-charged sample analysed for diffusible H in Fig. 2c had an intact oxide layer before the TDA test. However, when the oxide scale is removed (Fig. 2d), the peak temperature in the desorption curve decreases from approximately 673 °C to 423 °C, with desorption starting in below 100 °C. This indicates that the oxide contains hydrogen atoms inside the bulk alloy and creates a diffusion barrier at intermediate temperatures, rather than following the conventional H diffusion and trapping mechanisms.

Oxidation Behaviour

We conducted a detailed analysis of oxide scale evolution using SEM and SEM-EDX, comparing the oxide growth behaviour of H_2 combustion samples to that of H-free samples heat-treated in air at a similar temperature (~835 °C). A thin oxide layer (<50 nm) forms on the sample surface during low-temperature pre-oxidisation before flame exposure. With exposure to either the H_2-rich flame or air, continuous oxide growth is observed (Fig. 3a). After 8 hours, the oxide scale thickness is 319 ± 85 nm for combustion samples and 442 ± 133 nm for H-free samples, with the differences being within the margin of error, likely resulting from surface and oxide roughness. Oxide growth is reflected in the colouration of the scale, which changes from gold after pre-oxidation to black after 8 hours of high-temperature exposure.

Chemical composition maps of the oxides in both environments (Fig. 3c) show similar features and are also consistent with literature[16,17]: an outer Cr-rich oxide (most likely chromia) with distinct Cr-depletion zones below (Fig. 4), and dark Al-rich specks (attributable to intergranular alumina) below the Cr-rich oxide. A discontinuous Nb-enriched layer between the oxide scale and metallic substrate most likely corresponds to δ-Ni_3Nb particles, commonly observed in this alloy[18–23]. Additionally, Nb enrichment is seen deeper into the material as plate-like particles, which is also likely δ. Large, blocky precipitates possibly indicate the formation of carbides.

There are two notable differences between the oxide scale formed during H_2 combustion and in air (Fig. 3b): Firstly, compared to high-temperature air exposure, the oxide layer of flame-charged samples is more compact and dense, as indicated by the less "wavy" surface appearance. Secondly, the cross-section suggests a more fragmented layer with more visible cracks and some sub-surface voids in the combustion environment. This fragmentation may be a result of steam or other combustion products enhancing oxidation and leading to cracking and spalling, which are phenomena that are well established in literature for Cr_2O_3[12,13,24,25]. Cracking of the oxide layer can not only result in internal oxidation of less stable non-protective oxides, but can also offer more diffusion pathways for hydrogen into the sample[26,27]. Simultaneously, rapid cooling during argon quenching could introduce cracks due to thermal shock and decohesion from the bulk. Interestingly, the presence of voids should normally suggest higher Cr segregation, but the opposite is observed here[28].

Mechanical and microstructural changes

After confirming that oxides contain diffusible H within the material and prevent -or at least delay- desorption of H from the bulk, we strived to answer how this affects the alloy's mechanical properties. To address this, we conducted room-temperature tensile tests on samples in the following conditions:

1. *H-free*: Heat treatment was conducted in a furnace in an air environment at an average temperature of 835 °C for 8 hours, replicating the thermal profile during H_2 combustion.
2. *Electrochemical*: Samples underwent the same initial thermal treatment as H-free samples, followed by 14 hours of electrochemical charging at 75 °C. This process serves as a reference for evaluating the extent of possible H embrittlement and comparison against flame-charged samples.
3. *H_2 Flame*: H_2 combustion in an H_2-rich flame for either 1 hour or 8 hours at a surface temperature of between 800 °C and 830 °C.

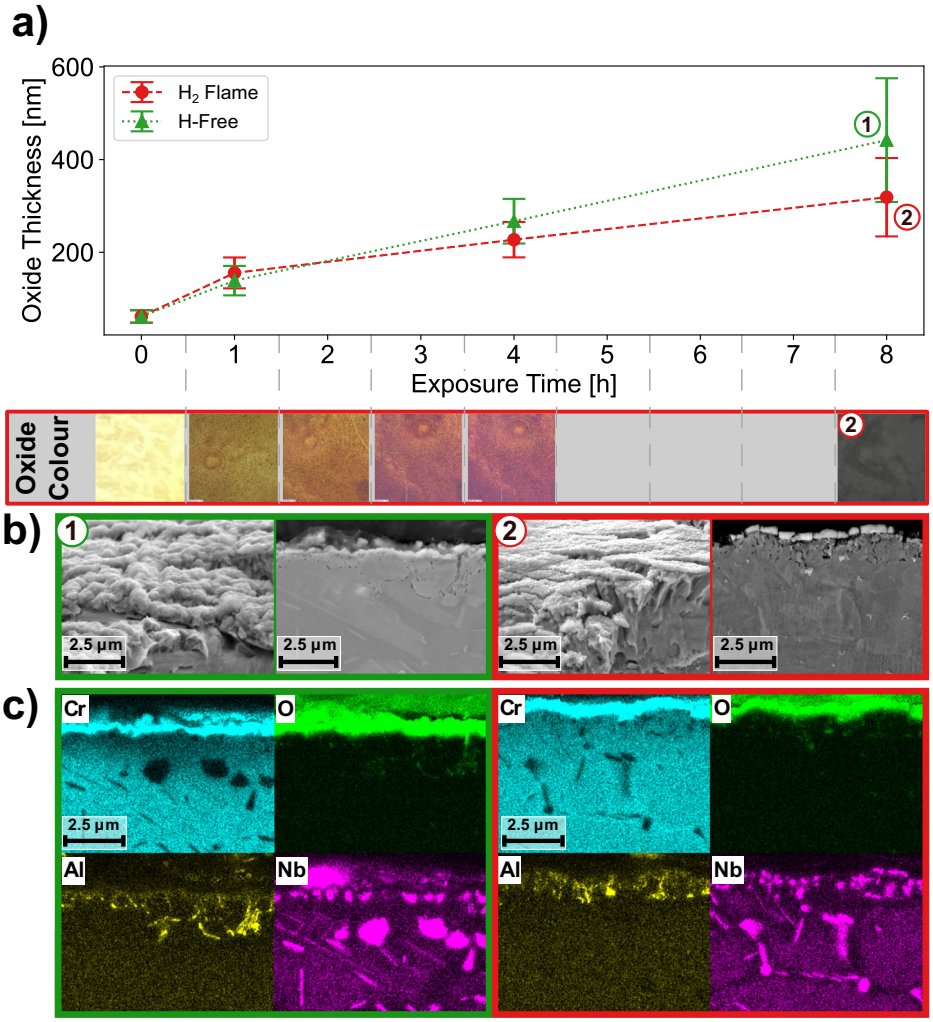

Fig. 3 | Oxide layer evolution over time. Change in oxide scale thickness and chemical composition for samples exposed to an H_2-rich flame (red) and high-temperature air (green). **a** Change in oxide layer thickness and colouration. **b** SEM characterisation of the oxide scale. **c** Chemical mapping using EDX. Error bars indicate measuring uncertainty due to local differences in oxide thickness.

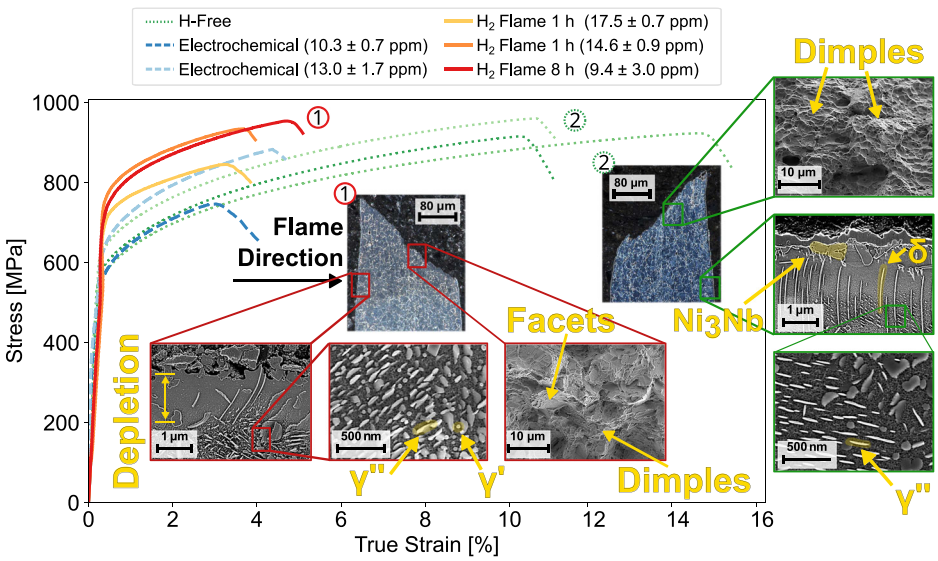

Fig. 4 | Mechanical Properties of Hydrogen-Charged Specimens. Tensile tests on samples exposed to an H_2-rich flame (orange), electrochemically charged (blue), and H-free (green) test pieces. Values in brackets are the total hydrogen measured after tensile testing. Cross-section of the fracture surface given for flame-charged and H-free samples. Micrographs reveal near-surface structure and strengthening phases. Fractography highlights differences in fracture mode between H-containing and H-free samples.

Fractographic and electron backscatter diffraction (EBSD) analyses were performed to investigate further differences in tensile behaviour between H_2 combustion and H-free samples. Although we strived for similar temperature profiles during flame and furnace exposure, we noticed γ' dissolution in H-free and electrochemically charged samples (micrographs in Fig. 4). This can occur at temperatures near 850 °C for this alloy[29], and also explain the small differences in the measured yield stress (Fig. 4). We note that the temperature difference alone may not explain entirely the differences observed in phase constituents and the impact of H on phase changes needs to be evaluated further. Nevertheless, the primary

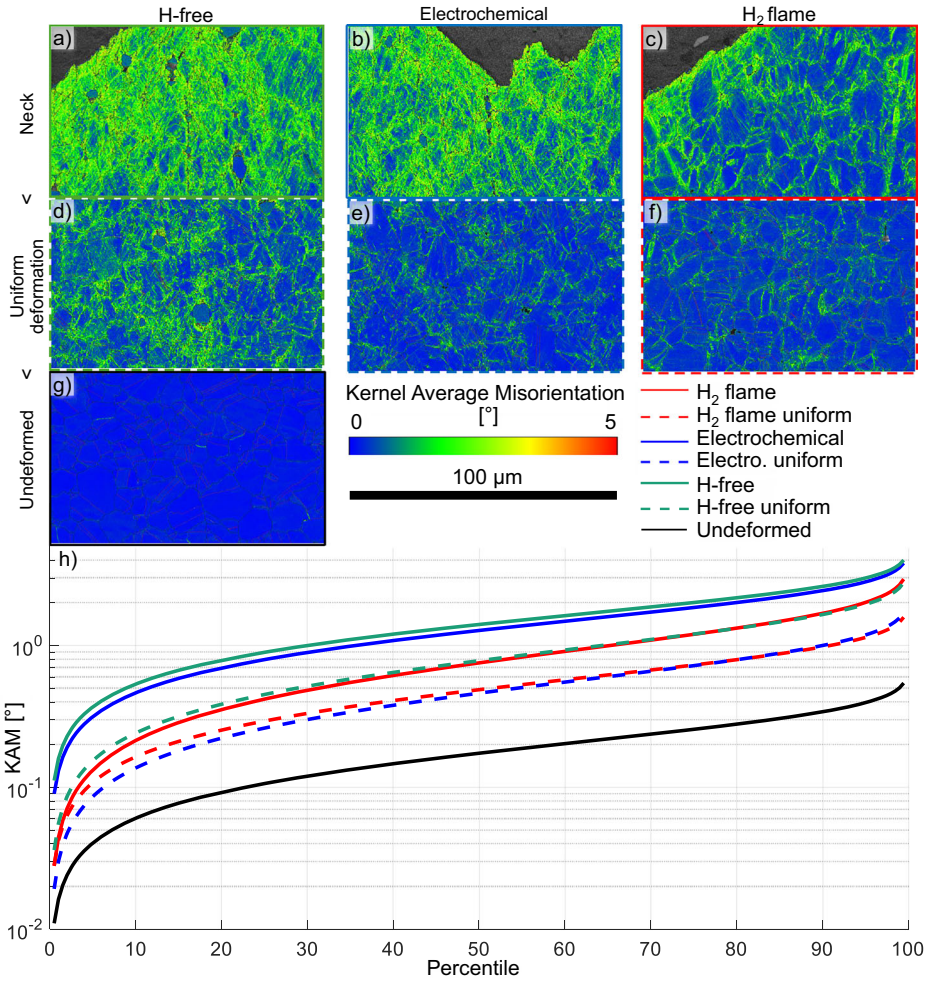

Fig. 5 | EBSD Analysis of Hydrogen-Charged Samples. Kernel average misorientation (KAM) analysis of tensile specimens deformed until fracture at the fracture site (neck) with the tensile direction oriented vertically and uniform deformation zone. Results for H-free samples are shown in (**a**) and (**d**); electrochemically charged samples in (**b**) and (**e**), and flame charged for 1 hour in (**c**) and (**f**). **g** shows results for an undeformed sample. **h** Shows the KAM distribution plots for all samples.

goal of the analysis is to investigate H embrittlement and as such, loss of ductility is deemed the more critical result and it will be shown that H embrittlement is not strongly controlled by the small differences in the final microstructure.

H-free reference samples demonstrate ductile fracture with a strain to failure of between 10% and 15%, as shown in Fig. 4. Fractography analysis shows a dimpled surface appearance with microvoids and transgranular fracture, indicative of ductile failure. This is further evidenced by EBSD analysis, where regions of high plastic strain are seen evenly distributed throughout the sample at the near-fracture region (Fig. 5a), as well as at the uniform deformation zone (several tens of micrometres away from the fracture region, Fig. 5d), showing strong signs of deformation strengthening, essential for higher ductility. Undeformed samples exhibit low and uniformly distributed average misorientation (Fig. 5g, h). This is indicative of a low or non-detectable density of geometrically necessary dislocations (GND).

Electrochemically H-charged samples exhibit a ~50% reduction in ductility compared to H-free samples, accompanied by slightly less deformation accumulated in the fracture region (Fig. 5b) and -more interestingly- less localised strain in the uniform deformation zone (Fig. 5e). Plastic strain is localised, therefore pointing towards significant hydrogen embrittlement. Although it is not readily possible to identify the specific hydrogen embrittlement mechanism(s) based on misorientation analysis, our findings are consistent with other literature pointing at hydrogen-enhanced localised plasticity (HELP) and/ or hydrogen-enhanced decohesion (HEDE)[30–33].

A different and unique behaviour is apparent in H_2 combustion samples: after 1 h in the H_2-rich flame, the loss in ductility is similar to the electrochemically charged samples. The fracture surface shows a facet-dominated morphology with very few voids or dimples. This is characteristic of brittle transgranular fracture, consistent with hydrogen embrittlement. However, the strain distribution near the fracture site is significantly less extensive, showing more "diffuse" regions close to planar shear bands and grain boundaries (Fig. 5c). This points towards the flame-charged sample having a more homogeneous distribution of hydrogen through the material compared to electrochemically H-charged ones. This is reinforced by the KAM distribution map extracted from each mapping (Fig. 5h), showing lower KAM values for the H_2 flame sample (solid red line). Further away from the fracture site (uniform deformation region, Fig. 5f), significant strain localisation is still present, but there is a more pronounced drop in strain (solid *vs* dashed red lines). For the uniformly deformed area, the average deformation distribution is very similar for both H-containing cases (dashed red and blue lines) and significantly smaller than in the H-free case (dashed green line). The higher curve slope for the electrochemically charged samples (blue dashed line) confirms the more localised deformation behaviour. This confirms that even if the macroscopic ductility loss is similar, the local deformation conditions leading to H embrittlement mechanisms can differ between the two charging methods, due to the difference in H distribution within the samples.

Discussion

Our custom-built hydrogen combustion rig for flame charging high temperature alloys with H provides unique capabilities to unveil hydrogen-metal interactions exclusive to H_2 combustion conditions. Adjusting fuel properties, flow rates, and sample position relative to the flame allows us to target distinct material and hydrogen flame interactions and accurately investigate how H_2 combustion affects material properties, which is not

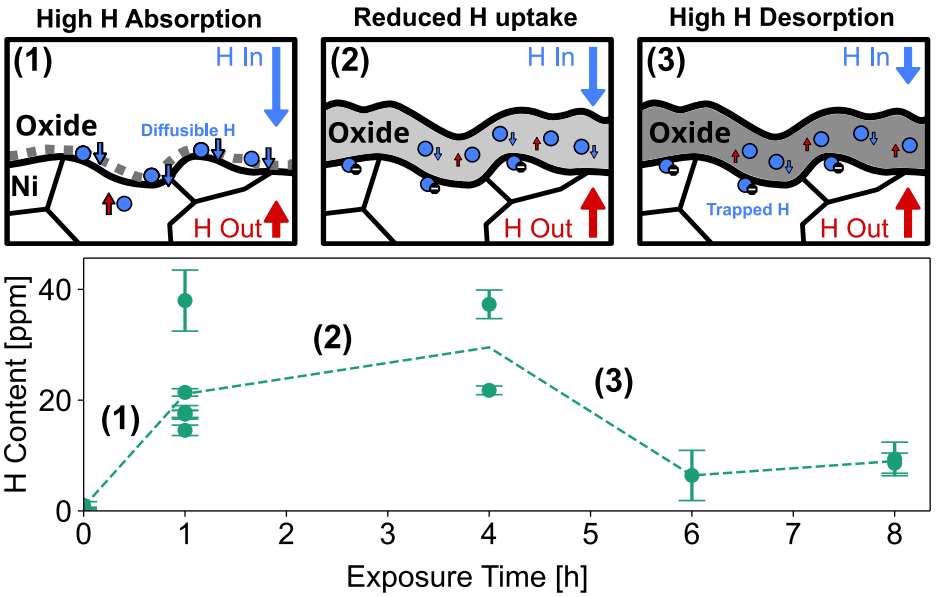

Fig. 6 | Hydrogen transport through oxide layers during Hydrogen combustion. Proposed kinematic mechanisms of hydrogen transport through oxide layers during (1) initial stages of oxide growth and transient oxide evolution - high hydrogen absorption; (2) Transient oxide stabilisation - first para-equilibrium between surface reactions for H absorption and desorption; (3) Formation of a more stable oxide as surface reaction balance shifts followed by a second para-equilibrium leading to lower bulk H concentration. Total hydrogen content over exposure time to H_2-rich flame is shown for thin sheet specimens. Error bars represent the measurement uncertainty from the TDA device.

possible with traditional hydrogen charging and testing methods. By simulating conditions that are relevant for future H_2 combustion engines, the setup allowed us to evaluate the feasibility of using existing Ni-base superalloys in these extreme environments. By argon quenching specimens immediately after the conclusion of the experiment, we can further ensure that virtually no hydrogen desorbs, thereby accurately capturing the material microstructure during combustion.

We found that hydrogen transport in the H_2-rich combustion environments is strongly influenced by surface oxide behaviour, as schematically illustrated in Fig. 6. An oxide layer formed prior to hydrogen flame charging increases hydrogen absorption within the samples, compared to oxide-free (polished) specimens (Fig. 2a). After 4 hours of H_2-flame charging, pre-oxidised samples are found to have a higher hydrogen concentration than oxide-free specimens. This is in clear contrast to previous literature, where oxides are described as hydrogen diffusion or desorption barriers only[34–37]. Although pre-oxidised samples also have a higher surface roughness than oxide-free counterparts, neither the literature[38–40] nor our own experiments (Supplementary Fig. 3) indicate that surface roughness would significantly increase hydrogen absorption. The H absorption curves in the flame charging environments (Fig. 2a, b, Fig. 6) follow a similar trend where hydrogen uptake is high in the first hour and is followed by an initial para-equilibrium stage. In sheet specimens, where surface effects are amplified, the maximum total hydrogen concentration (~30 ppm) drops significantly after 4 h to eventually converge at similar concentration ranges as in other sample conditions at 8 h. The reversal of hydrogen flux between 4 and 6 hours in sheet specimens -and between 1 and 4 hours in disc samples- clearly contradicts existing data from electrochemical or high-pressure hydrogen gas charging. Herein, hydrogen flux can usually be described mathematically with existing diffusion and trapping models, where H concentration continuously increases until saturation at the solubility limit of H in the material[41–45]. This finding is particularly critical, since a clear trend reversal would not be possible if the oxide forms only as a diffusion barrier; according to Sievert's law, it is impossible for the H content to suddenly decrease if the partial pressure and temperature are constant throughout the charging tests.

The role of the initial oxidation condition, i.e., pre-oxidised and oxide-free, on hydrogen absorption may be explained through the evolution of the oxide layers imposing continuously different energy barriers for absorption of all elements resulting from the combustion process: In oxide-free samples, residual oxides are removed before exposure to the H_2 flame, and therefore all oxides form at the testing temperature. The initial and unstable (transient) NiO spinel is relatively quickly replaced by more stable chromia[46–49]. For the pre-oxidised samples, a thin transient oxide layer is introduced on the surface during baking (heat treatment) at 550 °C in a nitrogen-rich atmosphere. The formation of oxides is well known to be strongly dependent on the environmental conditions[50–54]. Consequently, the oxide layer formed during baking very likely has a different chemical composition and crystal structure compared to the transient layer produced on the oxide-free sample during flame charging. This is especially relevant at the initial stages of oxide growth, as observed in Fig. 3, through the changes in oxide colouring. After a longer combustion duration, the differences in the initial oxide structure are expected to diminish, with both cases evolving to a similar, stable, and predominantly chromia top surface oxide. From a solubility standpoint, only the H activity at the top surface of the oxide is controlling the H absorption into the bulk alloy, as long as the exposure time is allowed to approach a dynamic equilibrium, i.e., steady state. The H activity and associated chemical reactions at the surface may be controlled by the flame (gas) composition and the oxide structure and orientation. For the case of catalytic H_2 combustion, an early study by Haruta and Sano[55] argued that oxide composition and crystal structure are the rate-determining factors for the hydrogen-oxidation activity; however, further evidence is required to confirm this. We assume that the oxide structure has a similar influence on the remaining surface reactions (Supplementary Eqs. A.1–A.6). This implies that, at a constant gas composition, the changes in oxide structure control the amount of H atoms dissociated and absorbed at the surface, possibly until reaching equilibrium (≥4h). This then determines the H activity at the surface and, as a consequence, the equilibrium H content in the bulk. The complex oxidation evolution proves the need for a broader understanding of the influence of the evolving surface condition on H adsorption, desorption, and H embrittlement. The crystal structure and specific composition of the oxides under hydrogen combustion environments need to be further characterised to fully understand their impact on hydrogen absorption.

Not only is hydrogen absorption during flame charging is governed by the oxide layers on the surface, but also H desorption. TDA results in oxide-free electrochemically charged samples show that the bulk of hydrogen is released below 350 °C with some amount already desorbing below 50 °C. In contrast, for the flame charged case, this peak shifts to above 600 °C but removing the oxide layer partially reverts this change (Fig. 2c). The difference in the desorption peak temperature between electrochemical and flame charging after removing the oxide layer can readily be explained by the H atoms being localised near the surface during aqueous H charging (Supplementary Fig. 4), as opposed to likely having more extensive H diffusion within the bulk in the flame charged samples. The hydrogen desorption

peak shifting to a higher temperature when the oxide layer is present can reasonably be explained by a lower hydrogen mobility in the oxide compared to the bulk[56–59]. In IN718 samples containing an oxide layer, we find that the highest amount of H desorbs below 900 °C and close to the sample's surface temperature during the H_2 combustion trials (Fig. 2b–d). As such, the majority of hydrogen is diffusible within both the material and the (stable) oxide layer during H_2-flame charging. Any change in the equilibrium between the H absorption and desorption rates is therefore likely to be reflected in the total H concentration, as H atoms can traverse the oxide scale despite the apparent reduction in mobility within the scale. The dual role of oxides, increasing H absorption while simultaneously slowing down the H desorption rate, creates a possible paradox for materials design as the formation of stable oxides is a key feature of corrosion-resistant Ni-Fe-Cr superalloys such as IN718 or IN625[20,21,26,47,60]. Especially Cr_2O_3 is known for its low formation speed, high stability, and resistance to forming pores and cracks[24,48,61–63], which give superalloys superior high-temperature corrosion resistance. Although we found no significant differences in the microstructure and chemical composition between H-free and H_2-flame charged samples, possible cracking and spalling of the oxide scale were found to be present after 8 hours in the flame.

Tensile testing following hydrogen combustion reveals that hydrogen that is contained in the bulk material contributes to H embrittlement in H_2-flame-charged samples. After only 1 h in the H_2-rich flame, IN718 is already severely embrittled, lowering its ductility by approximately 55% compared to air. This is a comparable amount to after 14 h of electrochemical H charging. While the extent of H embrittlement between electrochemical and flame charging is similar, EBSD analyses (Fig. 5a–h) show that marked differences exist between the two H_2-containing environments. Close to the fracture site, the extent of localised deformation is significantly weaker for the H_2-flame charged sample. Further away from the fracture site, i.e., at the uniform deformation zone, both H-containing samples show a similar decrease in total accumulated strain. The observed differences imply that hydrogen atoms are not trapped to the same extent in the H_2 flame as in electrochemical charging. This can be explained as hydrogen atoms absorbed during H_2-flame charging remain highly mobile at high temperatures, likely leading to a more homogeneous hydrogen distribution.

This work has defined new and exciting avenues for advanced studies of hydrogen in metals in H_2-flame charging environments. We demonstrate that the effect of individual degradation mechanisms on alloy performance, including H embrittlement or oxidation, must not be analysed separately but together, to fully capture the mechanisms governing material degradation in H_2 combustion. For example, while the role of water steam on oxide scales is well documented for Ni-base superalloys[11–13,25], its interplay with other sources of degradation, such as internal oxidation, nitridation and H embrittlement[64], is not yet known. Analysing oxide growth behaviour for longer combustion durations (>8 hours) could therefore yield valuable information on how this long-term interaction evolves. As we have shown, hydrogen uptake is strongly governed by oxide evolution and any changes in the oxide structure over longer durations, such as cracking or spalling, could significantly affect the bulk H solubility by changing the balance between hydrogen absorption and desorption. This does not only have strong implications for the fracture of components in H_2 combustion systems but also for creep and fatigue life. Only limited literature is available regarding the effect of hydrogen on these deformation modes[65–67], and, to our knowledge, no data exists about the combined effect of hydrogen and combustion-specific degradation on creep and fatigue. As resistance to these mechanisms is crucial for the longevity of jet engine components near the combustion chamber, our findings encourage careful reassessment of how current requirements for creep and fatigue in engine materials are defined. We also envision expanding the hydrogen combustion experiments to a wide range of thermomechanical conditions and more accurately evaluating the performance of Ni-base superalloys in future H_2 combustion conditions: Cyclic exposure tests will give insights into how frequent engine re-starts could affect oxide layer evolution and hydrogen uptake. Combustion tests in lean fuel conditions could shed light onto how the hydrogen-related damage mechanisms described in the previous sections change in more application-relevant conditions. Most importantly, insights gained from these studies will help the development of new materials and certification requirements for the safe operation of future H_2 combustion engines.

Conclusions

In summary, we present the following conclusions:

1. We have developed a unique hydrogen combustion setup to conduct systematic flame charging studies of nickel-base superalloys in realistic H_2 combustion environments. With this test rig, we can cover a wide range of engine-relevant combustion conditions in fuel-lean and fuel-rich conditions and up to sample temperatures of ~1200 °C. The setup is designed for fine adjustments to H_2, N_2, and air flows, along with continuous measurements of relevant testing parameters during combustion, ensuring consistent and reproducible conditions.
2. Oxides play a dual critical role during combustion. Pre-existing oxides likely control hydrogen surface adsorption and absorption, increasing H concentration by up to 133% after 4 hours of H_2-flame charging. At the same time, oxides also prevent H desorption at lower temperatures. The results are in agreement with early studies on H_2 catalytic combustion, suggesting that oxide structures can modify the surface reactions, therefore affecting the net hydrogen absorption and desorption rates. The current understanding of hydrogen transport phenomena from literature based on pure H_2 charging is therefore not applicable, as hydrogen uptake of oxidising samples exposed to a H_2 flame and the balance between H absorption and desorption of oxide-containing alloys are rarely considered.
3. The hydrogen desorption profiles in flame charging environments are not directly comparable to those from electrochemical hydrogen charging and the relevant literature. Oxide layers formed during combustion result in a shift in the peak H desorption temperature from ~300 °C to >650 °C, which could be "naively" attributed to strong hydrogen trapping after combustion when following standard H diffusion and trapping theory. However, removing the oxide layer after combustion lowers the peak temperature again. This phenomenon is likely a result of the significantly reduced H diffusivity in the oxide compared to the bulk. The material's surface condition must therefore be taken into account during testing and when comparing H_2 combustion data to previously established knowledge and experience from other hydrogen applications.
4. Hydrogen embrittlement can occur in H_2 combustion environments to a similar extent as during electrochemical charging, even after short exposure times. True strain to failure decreases from ~10% in H-free samples to ~4% in both electrochemically and flame-charged specimens. However, despite a similar loss in macroscopic ductility and total hydrogen concentrations, material deformation and fracture differ between electrochemical and flame charging conditions. While significant strain localisation exists near the fracture surface of both sample conditions, the extent of localised strain was much lower in the flame-charged sample, indicating more effective embrittlement. Moreover, the difference in strain localisation between fracture and uniform deformation regions was much smaller in flame-charged samples, confirming a more homogeneous H distribution. Consequently, localised regions of hydrogen embrittlement may develop more readily across flame-charged samples, even if they were mechanically loaded below the nominal fracture strains, but for longer times. The shift in the localised strain and fracture mechanisms between the two environments highlights the challenge of transferring knowledge from established hydrogen embrittlement evaluation methods to the new combustion engine environment despite showing similar macroscopic loss of ductility.
5. The unique hydrogen transport and damage mechanisms found in H_2 combustion pose new challenges for both alloy development and engine design. Defining material requirements for strength, creep, and

fatigue life in H_2 combustion systems cannot rely on established hydrogen charging methods. Instead, new material testing and characterisation approaches are needed that take into account the combined degradation from hydrogen and combustion-specific mechanisms, like those identified in this work. Surface protection mechanisms should be developed as H absorption barriers to keep alloy's H concentrations at safe levels, whilst avoiding the promotion of mobile hydrogen within the bulk. Existing thermal barrier coatings need to be re-evaluated for their influence on H dissociation, adsorption and retention. Engine design needs to consider the deleterious effects of hydrogen embrittlement and combustion products such as water steam or fuel impurities by optimising fuel-air ratios and adopting component geometries that reduce stress concentrations in hydrogen-rich regions. Together, these strategies can mitigate highly localised H embrittlement and increase the reliability of nickel-base superalloy components in future hydrogen combustion environments for safe and efficient H_2-powered jet engines.

Methods

Hydrogen flame charging is carried out using a custom-built hydrogen combustion test rig (Fig. 1). We mount samples in a spring-loaded, insulated Al_2O_3 holder to avoid possible interactions between the hydrogen flame and other metallic components. A thermocouple is integrated into the sample holder and continuously measures the temperature at the back of the sample during combustion. Hydrogen gas and air are supplied from stores to a nozzle where they are pre-mixed. As atmospheric air can interact with the hydrogen flame, thereby altering the flame properties, we incorporated a steady stream of nitrogen shielding gas into the nozzle assembly. Hydrogen, nitrogen, and air flow rates are set and continuously monitored with flow metres. We use high-pressure argon gas to rapidly cool down the sample following flame extinguishment to limit hydrogen desorption while the sample is still hot. Argon is unlikely to introduce hydrogen into the sample as other gases could do.

Samples were exposed to a pure hydrogen flame in fuel-rich conditions for 1–8 hours. Following flame charging, the mechanical performance of materials was evaluated using tensile testing and the amount of absorbed hydrogen was measured by thermal desorption analysis (TDA); total and diffusible H measurements were conducted using TDA. To isolate the effects of combustion-specific phenomena on hydrogen mobility, we compared the hydrogen release and strain distribution behaviour with that of an electrochemically charged sample; prior to charging the sample was heat-treated in an air furnace to mimic the thermal profiles followed during flame charging. Electrochemical charging is well established to evaluate the suitability of metals for applications in H-introducing environments, including aerospace[68–71]. Scanning electron microscopy (SEM) was used to evaluate microstructural changes in H_2 combustion samples and energy dispersive X-ray (EDX) was used to characterise oxide scales formed in hydrogen-rich and hydrogen-free environments. Electron backscatter diffraction analyses (EBSD) gave detailed insights into localised strain behaviour and aid in quantifying hydrogen embrittlement. The loss in ductility following combustion was compared to samples that were electrochemically charged and H-free reference samples, both of which underwent similar thermal histories as during flame exposure.

Data availability

The data that support the findings of this study are available from the corresponding author upon reasonable request.

Received: 21 July 2025; Accepted: 8 October 2025;
Published online: 21 November 2025

References

1. Douglass, H. W., Hennings, G. & Price, H. G. Experimental performance of liquid hydrogen and liquid fluorine in regeneratively cooled rocket engines. Technical Memorandum NASA-TM-X-87 (1959).
2. Fritzemeier, L.C. & Chandler, W.T. Hydrogen Embrittlement-Rocket Engine Applications. In (eds. Tien, J.K. & Caulfield, T.) *Superalloys Supercomposites Superceramics*, 491–524 (Academic Press, 1989).
3. Sosounov, V. & Orlov, V. Experimental turbofan using liquid hydrogen and liquid natural gas as fuel. In *the 26th Joint Propulsion Conference* (1990).
4. Westenberger, A. H2 Technology for Commercial Aircraft. In *Advances on Propulsion Technology for High-Speed Aircraft* (2008).
5. Johnson, W. H. On some remarkable changes produced in iron and steel by the action of hydrogen and acids. *Nature* **11**, 393 (1875).
6. Barrera, O. et al. Understanding and mitigating hydrogen embrittlement of steels: a review of experimental, modelling and design progress from atomistic to continuum. *J. Mater. Sci.* **53**, 6251–6290 (2018).
7. Lee, J. Hydrogen embrittlement of nickel, cobalt and iron-based superalloys. In (eds. Gangloff R.P. & Somerday B.P.) *Gaseous Hydrogen Embrittlement of Materials in Energy Technologies*, 624–667 (Woodhead Publishing, 2012).
8. Winter, C. Hydrogen in high-speed air transportation. *Int. J. Hydrog. Energy* **15**, 579–595 (1990).
9. Wright, I. & Gibbons, T. Recent developments in gas turbine materials and technology and their implications for syngas firing. *Int. J. Hydrog. Energy* **32**, 3610–3621 (2007).
10. Janakiraman, R., Meier, G. H. & Pettit, F. S. The effect of water vapor on the oxidation of alloys that develop alumina scales for protection. *Metall. Mater. Trans. A* **30**, 2905–2913 (1999).
11. Onal, K., Maris-Sida, M., Meier, G. & Pettit, F. The Effects of Water Vapor on the Oxidation of Nickel-Base Superalloys and Coatings at Temperatures from 700 C to 1100 C. In *Superalloys 2004 (Tenth International Symposium)*, 607–615 (2004).
12. Pint, B. A., Dryepondt, S. & Unocic, K. A. Oxidation of superalloys in extreme environments. In *Superalloy 718 and Derivatives*, 859–875 (2010).
13. Saunders, S., Monteiro, M. & Rizzo, F. The oxidation behaviour of metals and alloys at high temperatures in atmospheres containing water vapour: A review. *Prog. Mater. Sci.* **53**, 775–837 (2008).
14. Stefan, E., Talic, B., Larring, Y., Gruber, A. & Peters, T. A. Materials challenges in hydrogen-fuelled gas turbines. *Int. Mater. Rev.* **67**, 461–486 (2022).
15. Dreizler, A. & Böhm, B. Advanced laser diagnostics for an improved understanding of premixed flame-wall interactions. *Proc. Combust. Inst.* **35**, 37–64 (2015).
16. Wise, G. J. et al. Oxidation behaviour of new nickel-base superalloys with varying aluminium: Niobium ratio. *High. Temp. Corros. Mater.* **99**, 241–266 (2023).
17. Kang, Y.-J., Yang, S., Kim, Y.-K., AlMangour, B. & Lee, K.-A. Effect of post-treatment on the microstructure and high-temperature oxidation behaviour of additively manufactured Inconel 718 alloy. *Corros. Sci.* **158**, 108082 (2019).
18. Moddeman, W. E., Craven, S. M. & Kramer, D. P. Ni3Nb alloy species in oxide surfaces of INCONEL 718. *Metall. Trans. A* **17**, 351–355 (1986).
19. Pang, X., Dwyer, D., Gao, M., Valerio, P. & Wei, R. Surface enrichment and grain boundary segregation of niobium in inconel 718 single- and poly-crystals. *Scr. Metall. Mater.* **31**, 345–350 (1994).
20. Delaunay, F., Berthier, C., Lenglet, M. & Lameille, J.-M. SEM-EDS and XPS studies of the high temperature oxidation behaviour of inconel 718. *Microchim. Acta* **132**, 337–343 (2000).
21. Sanviemvongsak, T., Monceau, D. & Macquaire, B. High temperature oxidation of IN 718 manufactured by laser beam melting and electron beam melting: Effect of surface topography. *Corros. Sci.* **141**, 127–145 (2018).
22. Doleker, K. M., Odabas, O., Ozgurluk, Y., Askerov, H. & Karaoglanli, A. C. Effect of high temperature oxidation on Inconel 718 and Inconel 718/YSZ/$Gd_2Zr_2O_7$. *Mater. Res. Express* **6**, 086456 (2019).

23. Kruk, A. et al. Three-dimensional characterization of an oxide scale on ATI 718Plus® superalloy. *Corros. Sci.* **169**, 108634 (2020).
24. Lai, H. *High temperature oxidation and corrosion of Ni-based superalloys for industrial gas turbines*. Chalmers University of Technology, Göteborg, (2014).
25. England, D. M. & Virkar, A. V. Oxidation kinetics of some nickel-based superalloy foils in humidified hydrogen and electronic resistance of the oxide scale formed Part II. *J. Electrochem. Soc.* **148**, A330 (2001).
26. Pettit, F. & Meier, G. Oxidation and hot corrosion of superalloys. In *Superalloys 1984 (Fifth International Symposium)*, 651–687 (1984).
27. Li, Q. et al. Performances of Cr_2O_3-hydrogen isotopes permeation barriers. *Int. J. Hydrog. Energy* **40**, 6459–6464 (2015).
28. Li, L. et al. Influence of building direction on the oxidation behavior of Inconel 718 alloy fabricated by additive manufacture of electron beam melting. *Materials* **11**, 2549 (2018).
29. Slama, C., Servant, C. & Cizeron, G. Aging of the Inconel 718 alloy between 500 and 750 °C. *J. Mater. Res.* **12**, 2298–2316 (1997).
30. Birnbaum, H. & Sofronis, P. Hydrogen-enhanced localized plasticity-a mechanism for hydrogen-related fracture. *Mater. Sci. Eng. A* **176**, 191–202 (1994).
31. Troiano, A. R. The role of hydrogen and other interstitials in the mechanical behavior of metals. *Metallogr., Microstruct., Anal.* **5**, 557–569 (1960).
32. Oriani, R. A. A mechanistic theory of hydrogen embrittlement of steels. *Ber. der Bunsenges. f.ür. Phys. Chem.* **76**, 848–857 (1972).
33. Wan, D., Deng, Y., Meling, J. I. H., Alvaro, A. & Barnoush, A. Hydrogen-enhanced fatigue crack growth in a single-edge notched tensile specimen under in-situ hydrogen charging inside an environmental scanning electron microscope. *Acta Mater.* **170**, 87–99 (2019).
34. Turnbull, A. Hydrogen diffusion and trapping in metals. In (eds. Gangloff, R.P. & Somerday, B.P.) *Gaseous Hydrogen Embrittlement of Materials in Energy Technologies*, 89–128 (Woodhead Publishing, 2012).
35. Verbeken, K. Analysing hydrogen in metals: bulk thermal desorption spectroscopy (TDS) methods. In (eds. Gangloff R.P. & Somerday B.P.) *Gaseous Hydrogen Embrittlement of Materials in Energy Technologies*, 27–55 (Woodhead Publishing, 2012).
36. Hollenberg, G., Simonen, E., Kalinin, G. & Terlain, A. Tritium/hydrogen barrier development. *Fusion Eng. Des.* **28**, 190–208 (1995).
37. Wetegrove, M. et al. Preventing hydrogen embrittlement: the role of barrier coatings for the hydrogen economy. *Hydrogen* **4**, 307–322 (2023).
38. Shin, H.-S., Yeo, J. & Baek, U.-B. Influence of specimen surface roughness on hydrogen embrittlement induced in austenitic steels during in-situ small punch testing in high-pressure hydrogen environments. *Metals* **11**, 1579 (2021).
39. Réquiz, R., Vera, N. & Camero, S. Influencia del acabado superficial en la permeación de hidrógeno del acero API 5L-X52. *Rev. Metal.* **40**, 30–38 (2004).
40. Kim, J. et al. Roughening improves hydrogen embrittlement resistance of Ti-6Al-4V. *Acta Mater.* **220**, 117304 (2021).
41. Oriani, R. The diffusion and trapping of hydrogen in steel. *Acta Metall.* **18**, 147–157 (1970).
42. Crank, J.*The mathematics of diffusion*. (Oxford University Press, 2011).
43. Li, J., Oudriss, A., Metsue, A., Bouhattate, J. & Feaugas, X. Anisotropy of hydrogen diffusion in nickel single crystals: the effects of self-stress and hydrogen concentration on diffusion. *Sci. Rep.* **7**, 45041 (2017).
44. Galindo-Nava, E., Basha, B. & Rivera-Díaz-del Castillo, P. Hydrogen transport in metals: Integration of permeation, thermal desorption and degassing. *J. Mater. Sci. Technol.* **33**, 1433–1447 (2017).
45. Marchi, C., Somerday, B. & Robinson, S. Permeability, solubility and diffusivity of hydrogen isotopes in stainless steels at high gas pressures. *Int. J. Hydrog. Energy* **32**, 100–116 (2007).
46. Reed, R. C.*The Superalloys: Fundamentals and Applications*. (Cambridge University Press, 2006).
47. Giggins, C. S. & Pettit, F. S. Oxidation of Ni-Cr-Al Alloys Between 1000° and 1200 °C. *J. Electrochem. Soc.* **118**, 1782 (1971).
48. Birks, N., Meier, G. H. & Pettit, F. S.*Introduction to the High Temperature Oxidation of Metals*. (Cambridge University Press, 2006).
49. Stott, F. H., Wood, G. C. & Stringer, J. The influence of alloying elements on the development and maintenance of protective scales. *Oxid. Met.* **44**, 113–145 (1995).
50. Wright, I. G. & Dooley, R. B. A review of the oxidation behaviour of structural alloys in steam. *Int. Mater. Rev.* **55**, 129–167 (2010).
51. Jang, C. et al. Oxidation behaviors of wrought nickel-based superalloys in various high temperature environments. *Trans. Nonferrous Met. Soc. China* **21**, 1524–1531 (2011).
52. Luo, L. et al. Atomic origins of water-vapour-promoted alloy oxidation. *Nat. Mater.* **17**, 514–518 (2018).
53. Archana, M., Rao, C. J., Ningshen, S. & Philip, J. High-temperature air and steam oxidation and oxide layer characteristics of alloy 617. *J. Mater. Eng. Perform.* **30**, 931–943 (2021).
54. Latif, A., Ueda, M. & Takeyama, M. Oxidation behavior of a novel nickel-based alloy in air and steam at 1273 K for the oxygen-hydrogen combustion chamber. *High. Temp. Corros. Mater.* **101**, 203–224 (2024).
55. Haruta, M. & Sano, H. Catalytic combustion of hydrogen i-its role in hydrogen utilization system and screening of catalyst materials. *Int. J. Hydrog. Energy* **6**, 601–608 (1981).
56. Chen, C., Yu, H. & Zheng, S. First-principles study of hydrogen diffusion mechanism in Cr2O3. *Sci. China Technol. Sci.* **54**, 88–94 (2011).
57. Robertson, W. M. Hydrogen permeation and diffusion in inconel 718 and incoloy 903. *Metall. Trans. A* **8**, 1709–1712 (1977).
58. Jebaraj, J. J., Morrison, D. J. & Suni, I. I. Hydrogen diffusion coefficients through Inconel 718 in different metallurgical conditions. *Corros. Sci.* **80**, 517–522 (2014).
59. Xu, J., Sun, X. K., Liu, Q. Q. & Chen, W. X. Hydrogen permeation behavior in IN718 and GH761 superalloys. *Metall. Mater. Trans. A* **25**, 539–544 (1994).
60. Smialek, J. & Meier, G. High-Temperature Oxidation. In (eds. Sims, C.T. et al.) *Superalloys II*, 293–326 (Wiley-Interscience, 1987).
61. Chen, J. H., Rogers, P. M. & Little, J. A. Oxidation behavior of several chromia-forming commercial nickel-base superalloys. *Oxid. Met.* **47**, 381–410 (1997).
62. Kumar, L., Venkataramani, R., Sundararaman, M., Mukhopadhyay, P. & Garg, S. P. Studies on the oxidation behavior of Inconel 625 between 873 and 1523 K. *Oxid. Met.* **45**, 221–244 (1996).
63. Young, D. J. *High Temperature Oxidation and Corrosion of Metals*, (Elsevier Science, 2016).
64. Krupp, U. & Christ, H.-J. Selective oxidation and internal nitridation during high-temperature exposure of single-crystalline nickel-base superalloys. *Metall. Mater. Trans. A* **31**, 47–56 (2000).
65. Harris, J. A. & Vanwanderham, M. C. Properties of materials in high pressure hydrogen at cryogenic, room, and elevated temperatures. Technical Memorandum FR-5768 (1973).
66. Mucci, J. & Harris, J. Influence of gaseous hydrogen on the mechanical properties of high temperature alloys. Technical Memorandum FR-7746 (1976).
67. Chen, P., Vesely Jr, E. & Panda, B. The LCF Behavior of the Ni-Base Superalloy PWA 1489 in Hydrogen. In *Superalloys 1992 (Seventh International Symposium)*, 835–844 (1992).
68. Danford, M. D., Jeng, J. I. & Lower, J. R. An electrochemical study of hydrogen uptake and elimination by bare and gold-plated waspaloy. Technical Memorandum NASA TM-86479 (1984).
69. Murakami, Y., Kanezaki, T. & Mine, Y. Hydrogen effect against hydrogen embrittlement. *Metall. Mater. Trans. A* **41**, 2548–2562 (2010).

70. Lee, J. A. Hydrogen Embrittlement. Technical Memorandum NASA/TM-2016-218602 (2016).
71. Dwivedi, S. K. & Vishwakarma, M. Hydrogen embrittlement in different materials: A review. *Int. J. Hydrog. Energy* **43**, 21603–21616 (2018).

Acknowledgements

P.S. and E.G.-N. acknowledge the financial support of Reaction Engines Limited. We are grateful for the insightful discussions with Dr Caroline Goddard. P.S. and E.G.-N. are grateful for the insightful discussions with Rolls-Royce plc. D.D. and E.G.-N. acknowledge the Civil Aviation Authority (CAA) for the provision of funding and are grateful for the highly stimulating discussions with the "H challenge" team at the CAA. MT gratefully acknowledges funding from the UKRI towards his Future Leaders Fellowship (MR/T019735/1).

Author contributions

P.S. and D.D. conducted combustion experiments, performed hydrogen content studies, tensile tests, and microscopy analyses. P.S., D.D., N.R., C.E., E.G-N. R.B. and M.T. developed the hydrogen combustion setup. P.S., D.D., N.R., C.E., M.T., R.B., and E.G.-N. discussed and interpreted the results and analysis. P.S. and D.D. drafted the paper and figures. P.S., D.D., N.R., C.E., M.T., R.B., and E.G.-N. reviewed and edited the paper. M.T., R.B., and E.G.-N. supervised the study and obtained the funding for research.

Competing interests

The authors declare no competing interests.

Additional information

Supplementary information The online version contains supplementary material available at https://doi.org/10.1038/s43246-025-00988-9.

Correspondence and requests for materials should be addressed to Enrique Galindo-Nava.

Peer review information *Communications Materials* thanks Joon Sik Park and the other anonymous reviewer for their contribution to the peer review of this work. A peer review file is available.